



Sizes and Shapes of Sources in Solar Metric Radio Bursts

Mykola Gordovskyy¹, Eduard P. Kontar², Daniel L. Clarkson², Nicolina Chrysaphi^{2,3}, and Philippa K. Browning¹

¹Department of Physics & Astronomy, University of Manchester, Manchester M13 9PL, UK

²School of Physics & Astronomy, University of Glasgow, Glasgow, G12 8QQ, UK

³LESIA, Observatoire de Paris, Université PSL, CNRS, Sorbonne Université, Université de Paris, 5 place Jules Janssen, F-92195 Meudon, France

Received 2021 July 25; revised 2021 November 11; accepted 2021 November 13; published 2022 February 1

Abstract

Metric and decametric radio emissions from the Sun are the only direct source of information about the dynamics of nonthermal electrons in the upper corona. In addition, the combination of spectral and imaging (sizes, shapes, and positions) observations of low-frequency radio sources can be used as a unique diagnostic tool to probe plasma turbulence in the solar corona and inner heliosphere. The geometry of the low-frequency sources and its variation with frequency are still not understood, primarily due to the relatively low spatial resolution available for solar observations. Here we report the first detailed multifrequency analysis of the sizes of solar radio sources observed by the Low Frequency Array. Furthermore, we investigate the source shapes by approximating the derived intensity distributions using 2D Gaussian profiles with elliptical half-maximum contours. These measurements have been made possible by a novel empirical method for evaluating the instrumental and ionospheric effects on radio maps based on known source observations. The obtained deconvolved sizes of the sources are found to be smaller than previous estimations, and often show higher ellipticity. The sizes and ellipticities of the sources inferred using 2D Gaussian approximation, and their variation with frequency are consistent with models of anisotropic radio-wave scattering in the solar corona.

Unified Astronomy Thesaurus concepts: [Active sun \(18\)](#); [Radio bursts \(1339\)](#)

1. Introduction

The plasma density and magnetic field in the upper solar corona and inner heliosphere are not sufficient to produce detectable bremsstrahlung hard X-ray or gyrosynchrotron emissions. Hence, metric and decametric coherent radio emissions are the sole source of information about energetic electrons in these layers of the solar atmosphere (McLean & Labrum 1985; Dulk et al. 1998; Pick & Vilmer 2008; Klein et al. 2005; Reid et al. 2011). This information is vital to understanding the underlying mechanisms of electron acceleration and transport in the corona, and escape of energetic electrons from the corona into the heliosphere.

Metric and decametric radio emissions from the Sun are characterized by a myriad of various bursts with complicated frequency and spatial structure varying on tens of millisecond timescales (e.g., Warwick & Dulk 1969; Kundu 1982; Barrow et al. 1994; Sharykin et al. 2018; Kuznetsov & Kontar 2019; Chrysaphi et al. 2020; Magdalenic et al. 2020). Observing them requires sub-second temporal resolution in many narrow frequency bands. At the same time, spatial resolution is also extremely important, because knowing the locations and sizes of the low-frequency sources is essential for characterizing the physical properties of the emitting region, as well as the conditions in the corona and inner heliosphere, where radio emission propagates.

Radio waves in this spectral range are strongly affected by scattering and refraction in the turbulent solar corona (e.g., Bougeret & Steinberg 1977; Bastian 1994; Kontar et al. 2017). Recent years saw significant progress in low-frequency radio observation of the Sun and their theoretical interpretation. It has

been shown that sizes, locations, and temporal evolution of solar radio burst sources can be used as an important diagnostic tool for plasma turbulence in the solar corona and inner heliosphere (Kontar et al. 2017; Chrysaphi et al. 2018; Gordovskyy et al. 2019; Kontar et al. 2019; Chen et al. 2020). This has reignited interest in the question of the source sizes in solar radio bursts. However, although solar radio bursts have been intensively studied for the past six decades, there is no certainty regarding the sizes of the emission sources (e.g., Suzuki & Dulk 1985). This is because the relatively small interferometric baselines usually available for decametric solar radio observations, in combination with the need for high temporal cadence, result in a relatively low spatial resolution, making the evaluation of geometric properties of the sources very challenging.

There was a number of studies of the solar emission source sizes in the frequency range of 100 MHz–1 GHz. For instance, Mercier et al. (2006, 2015) used the combinations of Nancay Radioheliograph and Giant Meterwave Radio Telescope to map the radio emission from non-flaring Sun and found that between frequencies of 200 and 400 MHz the emission sources corresponding to active regions can be as little as 0'.5. However, only a handful of single-frequency observational estimations of source sizes in solar radio bursts are available at lower frequencies below 100 MHz. Abranin et al. (1976, 1978) found that the sizes of sources corresponding to individual stria in type III bursts normally have sizes between 20' and 40' at 25 MHz. Chen & Shawhan (1978) found similar sizes between about 25' and 40' in type III, as well as type II, IV, and V bursts observed at 26.4 MHz. More recently, Kontar et al. (2017) used the Low-frequency Array (LOFAR; van Haarlem et al. 2013) tied-array beam (TAB) data to investigate type III sources observed close to the center of solar disk. It was shown that at 32 MHz the major axis of the half-maximum contour of the source is about 19'. Murphy et al. (2021) used LOFAR data

Table 1

Characteristics of the Considered Solar Events, Showing Date and Time, Location in the Sky (Azimuth and Zenith Distance), and a Brief Description of the Event

Date	Time, UT	A	z	Type of Event
2015 Apr 16	11:55	188	47	Single type III
2015 Apr 27	12:25	200	49	Single type III
2015 May 6	11:48	188	53	Double type III
2015 Jun 20	12:01	198	60	Type IV
2015 Jun 25	11:46	185	60	Type II/IV
2017 Jul 12	08:52	118	46	Type III storm
2017 Jul 13	07:42	101	36	Single type III
2017 Jul 15	11:03	164	58	Type II, III
2017 Sep 9	11:17	176	42	Type IV?

Note. Azimuth A and elevation z are in degrees.

obtained in the interferometric mode to study a type III source observed off the solar limb. They found that at 35 MHz its shape can be approximated by an ellipse with the major and minor axes of about $18'$ and $10'$, respectively.

LOFAR is a state-of-the-art instrument that offers unprecedented opportunities to map solar radio emission with very high spectral and temporal resolution. In the TAB mode it provides data with high-frequency resolution (12 kHz) and temporal cadence (10 ms). However, the 3.5 km baseline normally used for solar TAB observations results in a relatively large point-spread function (PSF) or *dirty beam*, which is further affected by factors other than the instrument's baseline, such as the Earth's ionosphere. Hence, it is important to analyze LOFAR imaging data using an empirically obtained PSF, based on known source observations.

In this study, we develop a novel method to evaluate the effective PSF of a radio array using observations of a known source (i.e., a radio calibrator) at an arbitrary location. The method is then used to correct the intensity maps of solar radio bursts observed by LOFAR in the frequency range 30–45 MHz, and evaluate the sizes and shapes of sources observed in nine randomly chosen events.

2. Data and its Analysis

2.1. Observations

In this study we investigate nine randomly chosen solar radio bursts in the frequency range 30–45 MHz observed in 2015 and 2017. Spectral-imaging data for these events have been obtained using LOFAR in the tied-array beam mode. The considered solar radio bursts are of different types (Table 1), ranging from short-duration events containing a single type III burst (e.g., 2017 July 13 event) to long-duration type II and IV storms (e.g., 2015 June 20 and 2017 July 12 events). At the same time, characteristics of their dynamic spectra, such as the relatively narrowband emission ($\Delta f/f \approx 0.1\text{--}0.3$) and fast frequency drift of individual elements of dynamic spectra, indicate that the emission in all considered events is produced by the plasma mechanism (Ginzburg & Zhelezniakov 1958). Some of these bursts have been studied in more detail in recent years (e.g., Kontar et al. 2017; Chrysaphi et al. 2018, 2020; Chen et al. 2020). In each of the studied solar events we chose a moment corresponding to a bright feature in the dynamic spectrum.

In addition to solar radio data, in order to evaluate the effective PSF of LOFAR, the ionospheric refraction at different

frequencies, and estimate the value of ionospheric shift, we consider observations of a calibrator, i.e., a known compact radio source. Namely, we use 24 individual Tau A spectral-imaging observations obtained in the same frequency range, 30–45 MHz, using the same LOFAR observing mode. These 24 observations were obtained during 2017 July–September with the object at different coordinates $[A, z]$, with elevations over the horizon (or altitudes) ranging from $15^\circ\text{--}60^\circ$.

For solar spectral-imaging data obtained during 2015 April–June, 169 beams were used, while for solar and Tau A observations during 2017 July–September, 217 beams were used. The average spacing between beams was about $400''$.

The data obtained for the nine solar radio bursts and for the 24 individual Tau A observations has been preprocessed using the same procedure. First, the data has been degraded to temporal resolution of 1.6 s and to a frequency resolution of 320 kHz. From that point the data is treated individually for 16 frequency channels, from 30–45 MHz with 1 MHz step. The integration time for imaging is 2 s, for both solar and Tau A observations.

For each frequency channel, a constant background I_b has been subtracted from the data, with I_b calculated as the average between the faintest N beams, with N being equal to half the number of available beams. For instance, for the data defined using 217 beams, the 109 faintest beams are selected and the average value between them is assumed to be I_b . This is based on the assumption that in at least half of the field-of-view area, the real signal is not greater than the noise.

The initial analysis of spectral-imaging data described above yields apparent radio intensity maps $I_d(f, A, z)$, which are affected by instrumental and ionospheric effects. In the first approximation, the apparent maps $I_d(f, A, z)$ can be considered as convolutions of the real maps $I_0(f, A, z)$ with the PSF $\mathcal{F}(f, A, z, \Delta A, \Delta z)$, and shifted by $\Delta z_{\text{ir}}(f)$ due to radio-wave refraction in the Earth's ionosphere:

$$I_d(f, A, z) = I_0(f, A, z - \Delta z_{\text{ir}}(f)) * \mathcal{F}(f, A, z, \Delta A, \Delta z), \quad (1)$$

where A and z are the azimuth and zenith distance ($z = 90^\circ - a$, where a is the elevation). Therefore, to evaluate the actual location and shape of the observed object $I_0(f, A, z)$, one needs to deconvolve the dirty map, reducing it for the effect of the PSF, and shift it by Δz_{ir} . For this purpose, we empirically evaluate the effective PSF of LOFAR (Section 2.2) and the value of ionospheric shift at these frequencies (Section 2.3).

In this study it is assumed that the source intensity distributions are represented by 2D Gaussian profiles with elliptical half-maximum contours:

$$U(x, y) = U_0 \exp \left(- \frac{[(x - x_0) \cos \theta + (y - y_0) \sin \theta]^2}{a^2} - \frac{[(y - y_0) \cos \theta - (x - x_0) \sin \theta]^2}{b^2} \right),$$

where U_0 is the amplitude, x_0 and y_0 are coordinates of the maximum, $2\sqrt{\ln 2} a$ and $2\sqrt{\ln 2} b$ are the major and minor axes of the ellipse corresponding to the half-maximum contour, and θ is the tilt angle of that ellipse. Obviously, the real intensity distributions are likely to be more complex than 2D Gaussian distributions. We make this assumption in order to

regularize the observed and derived intensity distributions and avoid spurious results.

2.2. Effective PSF of LOFAR in TAB Mode

The observed maps of Tau A are convolutions of its actual shape and the LOFAR PSF (or dirty beam) (Equation (1)). Since the actual shape of Tau A is known, one can evaluate the shape of the PSF at different frequencies by deconvolving dirty Tau A maps, yielding the effective PSF shapes for the locations $[A, z]$, where Tau A was observed.

Deconvolution of Tau A maps has been performed using an iterative algorithm based on the modified method of Burger and van Cittert described by de Jager & Neven (1966). For the apparent intensity distribution I_d formed by the convolution of the actual intensity distribution I_0 and the PSF F

$$I_d = I_0 \star F$$

with I_0 known, the first iteration for the PSF F can be found as

$$F_1 = 2I_d - I_d \star I_0.$$

Each following iteration is calculated as

$$F_{p+1} = F_p + I_d - F_p \star I_0.$$

The iterations are performed until the difference between P th and $(P + 1)$ th iterations is negligible. Since the apparent shape of Tau A observed by LOFAR is much bigger than the actual Tau A shape, and therefore its detailed structure is not important, for the purpose of this deconvolution the actual Tau A shape (I_0) is represented by a 2D Gaussian. Parameters of the analytical function representing the Tau A intensity distribution are obtained by fitting a 2D Gaussian shape to the Tau A intensity map from Maloney & Gottesman (1979).

Obviously, in order to deconvolve the images of solar events, the PSF needs to be determined for the location of the Sun at the time of the event. To do this, we developed a PSF translation procedure, which makes it possible to evaluate the PSF for an arbitrary location in the sky based on the shape of PSF in another arbitrary location. This procedure is based on the assumption that all antennas of the interferometer are located in the horizontal plane and the locations are fixed.

Assume that the PSF corresponding to a source located at zenith has a form of

$$\mathcal{P}_z = f(A, z),$$

where A and z are the azimuth and zenith distance, respectively (Figure 1). This PSF function can be rewritten as a function of small angles ΔA and Δz as

$$\mathcal{P}_z = f(A_1, \Delta A, \Delta z), \quad (2)$$

where $\Delta A = z \sin(A - A_1)$ and $\Delta z = z \cos(A - A_1)$, and A_1 is some arbitrary azimuth. As the size of the object (i.e., values of ΔA and Δz) is assumed to be small, the small angle approximation can be used.

For an object observed away from zenith, the PSF will expand in the zenith angle direction because of the effective baseline contraction due to the projection effect:

$$\mathcal{P}_1 = f(A_1, z_1, \Delta A, \Delta z / \cos(z)). \quad (3)$$

For small values of ΔA and Δz and $z_1 \gg \Delta z$, the full azimuth and zenith angle can be calculated for every point on the maps

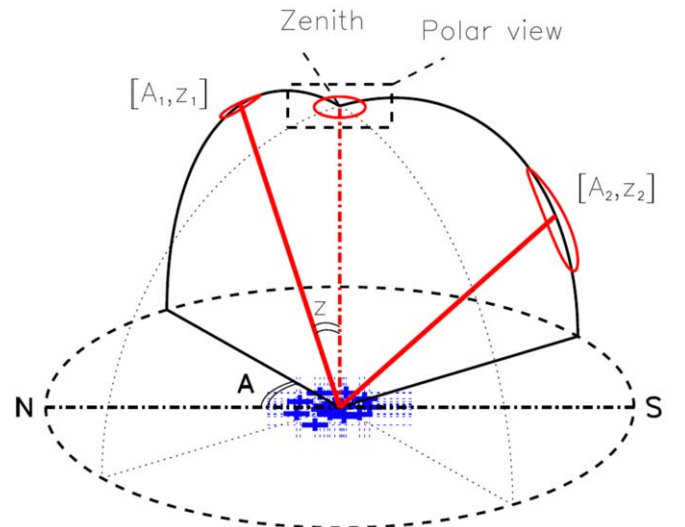


Figure 1. Sketch demonstrating the PSF translation procedure and the main parameters used in it.

as

$$A = A_1 + \Delta A / \sin(z), \quad (4)$$

$$z = z_1 + \Delta z. \quad (5)$$

Therefore, if the PSF of an instrument is known at zenith, Equations (2)–(5) can be used to predict the PSF for any arbitrary location in the sky A_1, z_1 , and vice versa. This, in turn, means that if the PSF is known for a location A_1, z_1 , it can be evaluated for another arbitrary location A_2, z_2 . Since the apparent intensity distribution corresponding to a point-like source should be equal to the PSF of an instrument, observing a point-like source in an arbitrary location in the sky makes it possible to evaluate the PSF for any other arbitrary location in the sky using Equations (2)–(5).

In order to test the developed method, we compare the PSFs derived using Tau A observations in one location in the sky with maps of Tau A observed in a different location. Figure 2 shows Tau A maps observed on the 2017 September 9 2017 about 36° over the horizon and PSFs derived for this particular location in the sky based on Tau A observed about 45° over the horizon on the 2017 July 13 (the intrinsic size of Tau A is significantly smaller than the observed sources and therefore, the maps shown in Figure 2 are determined primarily by the instrumental PSF). Although the Tau A maps observed on July 13 and September 9 are very different, Tau A maps observed on September 9 and the PSFs calculated for this particular observation based on July 13 observations are very similar, both in terms of the main lobe shapes and locations, and relative intensities of the side lobes.

The above analysis demonstrates that the PSF translation procedure works well for LOFAR observations in TAB mode. It also demonstrates that the quality of calculated PSFs heavily depends on the quality of the known object observations used to calculate the PSF. Therefore, to enhance the quality of the PSF maps, we calculate them using multiple observations of a known source. Thus, in this study we combine 24 different Tau A observations to evaluate the PSF at zenith (with respect to the array) for frequencies 30–45 MHz. The obtained PSFs are

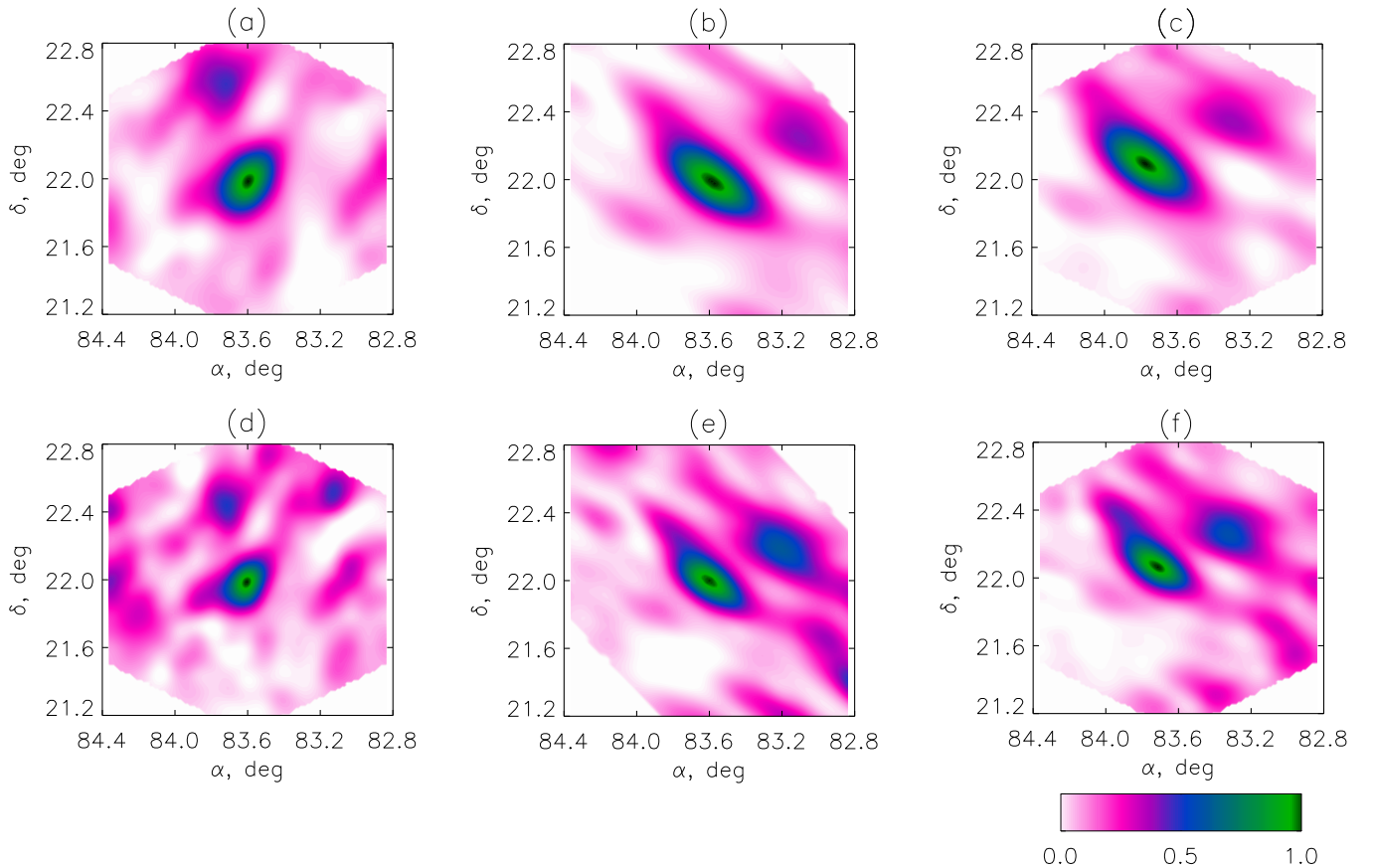


Figure 2. Left panels (a) and (d) show Tau A observed by LOFAR at 07:00 UT on 2017 July 13. Middle panels (b) and (e) show these intensity maps translated to the location where Tau A is observed at 10:05 UT on 2017 September 9. Right panels (c) and (f) show actual intensity maps of Tau A observed at 10:05 UT on 2017 September 9. Upper panels (a)–(c) correspond to the frequency 30 MHz, while lower panels correspond to 45 MHz.

then averaged for each individual frequency, yielding combined PSFs of the instrument (Figure 3).

The effective average PSF of LOFAR consists of the bright main lobe and a series of side lobes, forming an approximately hexagonal pattern. The side lobes become more prominent with increasing frequency and as expected, their distance from the main lobe centroid varies with frequency approximately as $1/f$. The sidelobe pattern appears to be asymmetric: side lobes located at azimuths 270° – 360° are bright, while side lobes located at azimuths 90° – 180° are practically impossible to detect.

Most importantly, the effective PSF appears to be significantly bigger than the nominal PSF for this mode of observations. Thus, at 30 MHz the area within the half-maximum contour of the nominal PSF corresponding to zenith is 110 arcmin^2 , while for the effective PSF derived using Tau A observations it is about 170 arcmin^2 .

This difference is also demonstrated by Figure 4, which shows Tau A observed by LOFAR at 30 MHz at 07:00 UT on 2017 July 13 compared with the nominal PSF of the instrument calculated for the same frequency, time, and α and δ coordinates. Since Tau A is significantly smaller than LOFAR PSF at this range of frequencies, one can expect the two maps to be very similar. Clearly, they are not: the main lobe area of the empirically derived PSF is about 1.6 times bigger than the main lobe area of the nominal PSF. Furthermore, unlike the empirically derived PSF, the nominal PSF shows much fainter, symmetric side lobes.

2.3. Ionospheric Shift

Metric radio emission is strongly affected by refraction in the Earth’s ionosphere, resulting in a shift of apparent positions of radio sources. These shifts can be considered as a sum of constant and variable components, with the latter varying on a range of timescales from minutes to months.

Comparison of the apparent location of Tau A with its known coordinates makes it possible to evaluate the shift for different frequencies and different elevations. Figure 5(a) demonstrates the effect of average ionospheric shift. As expected, it quickly increases with zenith distance: at 30 MHz the ionospheric shift is smaller than $0^\circ 03$ ($100''$) at about 60° over the horizon, increasing to almost $0^\circ 4$ at about 15° over the horizon.

The average shift should scale with the radio frequency as $\sim f^{-2}$, and hence, can be written as $\Delta z_{\text{ir}}(f, z) = f^{-2} \mathcal{R}(z)$. Fitting an analytical function to the position deviations normalized by $\sim f^{-2}$ (shown as a black line in Figure 5a) provides the best fit for the function $\mathcal{R}(z)$, yielding an empirical formula for the shift:

$$\Delta z_{\text{ir}}(z) = \frac{5.59}{f^2} \left[13.01 \exp\left(\frac{z - 44.417}{17.313}\right) - 1 \right], \quad (6)$$

where z and Δz_{ir} are in degrees and f is in megahertz. This formula is used to correct the observed intensity maps for the average ionospheric refraction shift.

Figure 5(a) represents the constant component of the ionospheric refraction shift for June–September season.

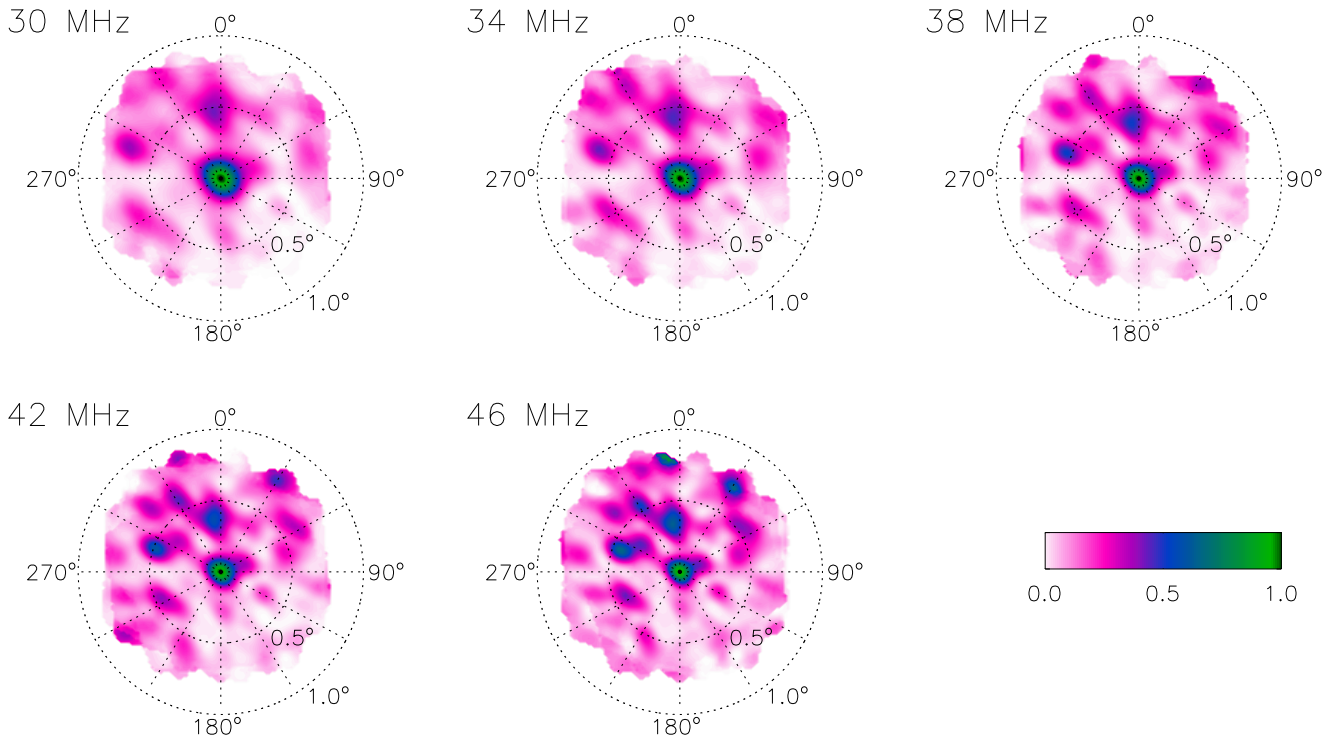


Figure 3. LOFAR PSF based on 22 Tau A observations projected to zenith above the LOFAR core. Frequencies are shown above the panels.

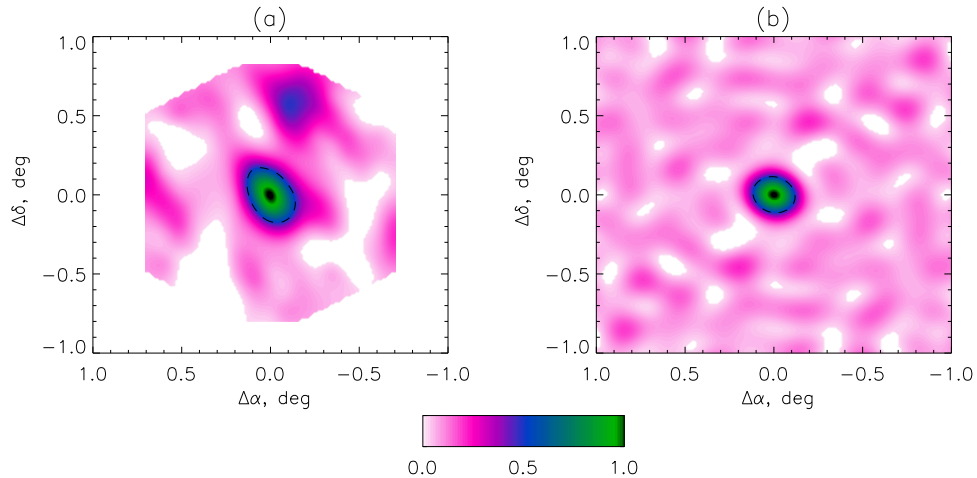


Figure 4. Tau A observed by LOFAR at 30MHz at 07:00 UT on 2017 July 13 compared with the nominal PSF of LOFAR calculated for the same frequency, time and sky coordinates.

However, the variable component of refraction is important too. Figures 5(b) and (c) demonstrate the effect of refraction on the apparent position for Tau A observed about 60° over the horizon at the frequency of 30 MHz. The variations with an amplitude of about $100''$ and a timescale of about 50–100 s most likely represent fast variations in the Earth’s ionosphere. Variations on longer timescales can be significant, with 5–20 minute variations caused by ionospheric gravity waves being most significant, with amplitudes of arcminutes (Mercier & Jacobson 1997).

In order to correct solar source positions for the effect of the variable refraction, one needs nearly simultaneous observations of several known bright objects with the positions in the sky relatively close to the Sun. Since finding such objects in the sky

is nearly impossible, we do not correct for the effect of these slower ionospheric variations, and therefore, they contribute to the position uncertainty. This uncertainty is represented by deviations of the observed positions from the average value (black line in Figure 5(a)). For the considered frequency range this uncertainty is about $100''$ – $150''$ (Gordovskyy et al. 2019).

Figures 5(b) and (c) also reveals fast oscillations with the amplitude of about $30''$ on the timescale of few seconds. These variations represent the error of centroid position measurements determined primarily by the characteristics of the TAB array used for observations. Since they occur on periods shorter than the integration time, they enhance the apparent area of the instrument’s PSF and solar sources and therefore, are accounted for during the deconvolution procedure.

3. Sizes and Shapes of Solar Radio Sources

3.1. Deconvolution of Solar Radio Images

The image deconvolution procedure, or cleaning, for each individual solar observation at each frequency consists of two parts: calculation of the PSF and then actual deconvolution. The PSF is calculated using the combined PSF discussed in Section 2.2. For each frequency the PSF is translated from zenith to the sky coordinates (A, z) , corresponding to the location of the Sun at the considered time using Equations (2)–(5). The coordinates of the map are corrected for the effect of ionospheric refraction: its equatorial coordinates are shifted so that its zenith distance z increases by the value calculated using Equation (6).

Deconvolution of the observed solar intensity maps (or *cleaning*) is done using the CLEAN algorithm (Högbom 1974; Hurford et al. 2002). This algorithm is based on the assumption that the real intensity map (or *real image*) can be represented by a linear combination of a variable background and a set of point-like sources. Convolved with the PSF, the real image yields the observed intensity map, or dirty image. The CLEAN algorithm iteratively calculates the locations and intensities of the point-like sources, producing the *clean component map* and the residual variable background map. Since the map of clean components is noisy (which is inevitable since deconvolution is a classical ill-posed problem), the result of the clean component map is usually convolved with the *clean beam*, which usually represents the main lobe of the corresponding PSF with side lobes removed. The clean components map convolved with the clean beam and added to the map of residuals yields the *clean image*, and is done purely for representation purposes. Therefore, the difference between the dirty maps and clean maps produced by the CLEAN procedure is that the clean maps are free from artefacts caused by the side lobes, while the apparent sizes of sources remain practically the same.

Deconvolution for one of the considered events is shown in Figure 6. It starts with the dirty images with the constant background subtracted (Figure 6(b), (c)). The PSF for the event (Figure 6(d), (e)) is derived using the combined PSF, as described in Section 2.2. The CLEAN procedure yields the clean component maps (Figure 6(f), (g)). The clean images are obtained by convolving the clean components with the clean beam, which is derived by fitting a 2D Gaussian to the main lobe of the PSF (Figures 6(h), (i)).

Since our aim is to evaluate the intrinsic sizes of the sources, we are interested in the clean component maps, rather than the clean images. In order to evaluate the sizes and shapes, the clean component maps are fitted with 2D Gaussian distributions for each frequency. This is done using the regularization procedure described below.

3.2. Fitting the Clean Component

Since the map of clean components is very noisy, the fitting algorithms often fail to converge or produce obviously false results in most cases. In order to overcome this problem, we introduce regularization into clean component fitting as follows. First, we convolve the map of clean components with \mathcal{F}_r —a 2D Gaussian distribution with the diameter of half-maximum contour w_r . The brightest source at the obtained map is then fitted with \mathcal{F}_c —a 2D Gaussian distribution, located at $[x_c, y_c]$ with major and minor axes of its half-maximum ellipse A_c and B_c , respectively, and tilt θ_c , the angle between the major

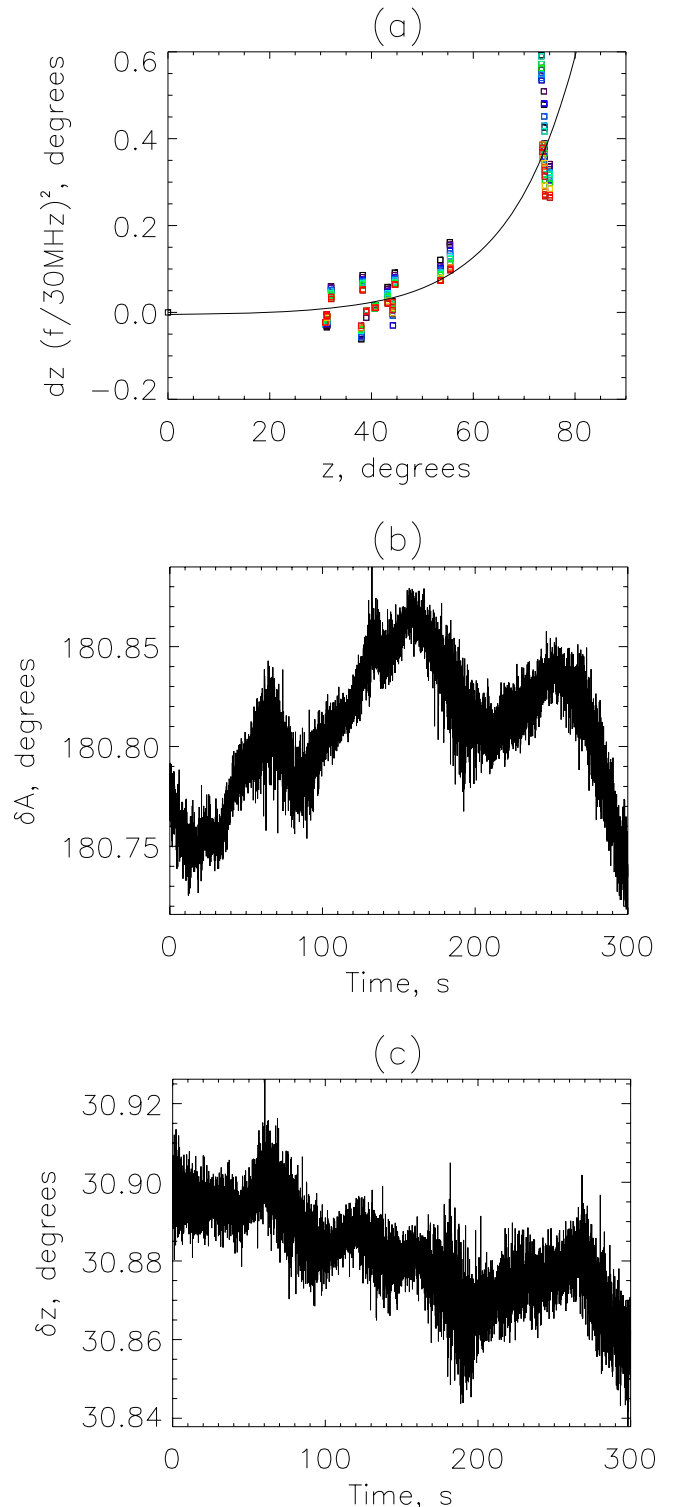


Figure 5. Panel (a) zenith distance offsets of Tau A centroids observed at different zenith distances. The values are normalized by f^2 factor to remove the effect of frequency variation (see Section 2.3). Different colors represent different frequencies from 30 MHz (black) to 48 MHz (red). The black line shows the analytical approximation for the $\mathcal{R}(z)$ function. Panels (b) and (c) apparent azimuth and zenith distance of Tau A observed at 30 MHz with the motion due to the Earth rotation removed. Horizontal axis shows the time after 11:01 UT on 2017 July 12.

axis and X -axis measured clockwise. Since \mathcal{F}_c represents convolution of \mathcal{F}_r with the intensity distribution in the intrinsic source \mathcal{F}_s , and \mathcal{F}_c and \mathcal{F}_r are 2D Gaussians, \mathcal{F}_s is also 2D

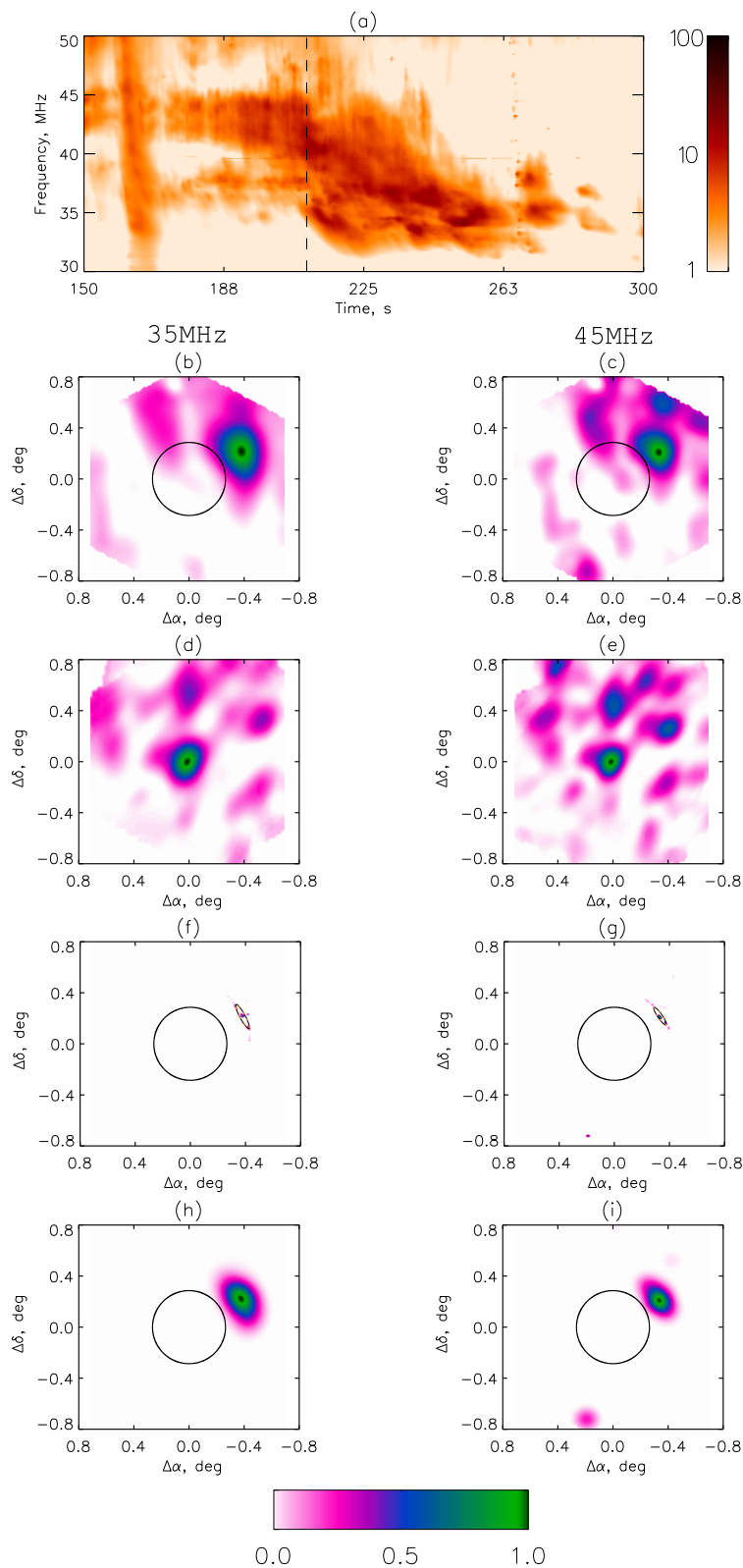


Figure 6. Solar radio map deconvolution procedure. Panel (a) shows the dynamic spectrum, the logarithm of intensity vs. time and frequency, for the considered event (a *transitioning* type II burst, reported by Chrysaphi et al. (2020)), with the X -axis showing time in seconds after 10:59:38 UT on 2017 July 15. Panels (b) and (c) show dirty maps observed at 11:03:07 UT (shown as the black dashed line in panel (a)). Panels (d) and (e) show corresponding LOFAR PSFs derived using the combined PSF for the location of the Sun at the moment of observations. Panels (f) and (g) show corresponding clean component maps (color scales, Section 3.1) and their 2D Gaussian fits (black and orange dashed lines show their half-maximum contours, Section 3.2). Panels (h) and (i) show corresponding cleaned maps (as described in Section 3.1). Panels (b), (d), (f), and (h) are for 35 MHz; panels (c), (e), (g), and (i) are for 45 MHz.

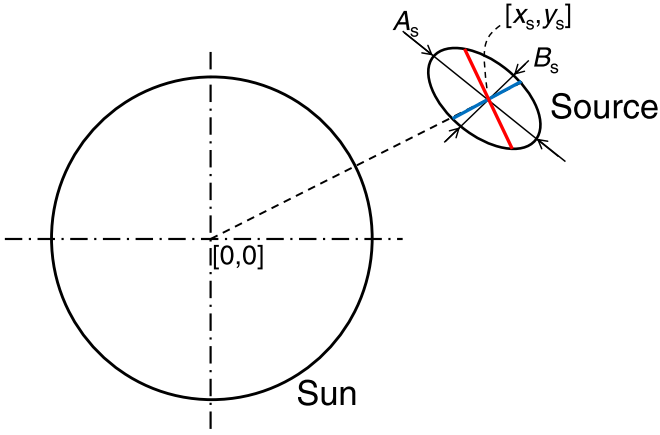


Figure 7. The sketch showing how the radial (blue line) and tangential (red line) sizes are defined, based on the location, and major, and minor axes of the ellipse, corresponding to the half-maximum contour of the 2D Gaussian representing the intrinsic source.

Gaussian and its parameters can be evaluated using the well-known Gaussian convolution rule. Hence, \mathcal{F}_s is a 2D Gaussian with major and minor half-maximum axes

$$A_s = \sqrt{A_c^2 - w_r^2}, \quad (7)$$

$$B_s = \sqrt{B_c^2 - w_r^2}, \quad (8)$$

respectively, with the same centroid location, $[x_s, y_s] = [x_c, y_c]$, and same tilt angle of its half-maximum ellipse, $\theta_s = \theta_c$.

Similar to most other studies, by the shape of a source we mean the ellipse corresponding to 0.5 of the intensity of the fitted 2D Gaussian distribution. Using the obtained fit parameters, we calculate the average sizes of the sources as

$$L_a = \sqrt{A_s B_s}. \quad (9)$$

The sizes of sources in radial direction (i.e., measured along the line connecting the source centroid and the center of the solar disk, Figure 7) and tangential directions (i.e., perpendicular to the radial directions) are calculated as

$$L_r = \frac{A_s B_s}{\sqrt{(A_s \sin(\theta_s - \lambda))^2 + (B_s \cos(\theta_s - \lambda))^2}}, \quad (10)$$

$$L_t = \frac{A_s B_s}{\sqrt{(A_s \cos(\theta_s - \lambda))^2 + (B_s \sin(\theta_s - \lambda))^2}}, \quad (11)$$

respectively, where $\lambda = \arctan(y_s/x_s)$.

3.3. Uncertainty of Solar Source Size Measurements

The uncertainties in the source sizes evaluated using the approach described in Section 3.2 have been estimated using synthetic data. A large number (10^3) of synthetic sources with 2D Gaussian distributions were generated with randomly chosen centroid locations, major and minor half-maximum axes, and tilt angles (angles between the major axes and horizontal axis). The synthetic sources were convolved with the actual LOFAR PSF, and reduced on an irregular grid identical to the LOFAR beam grid, with random noise (~ 0.1 of the source amplitude) and constant background (~ 10 – 20 of the source amplitude) added, creating synthetic dirty maps. The obtained *dirty maps* were then analyzed using the same procedure as described in Section 2 and Sections 3.1 and 3.2.

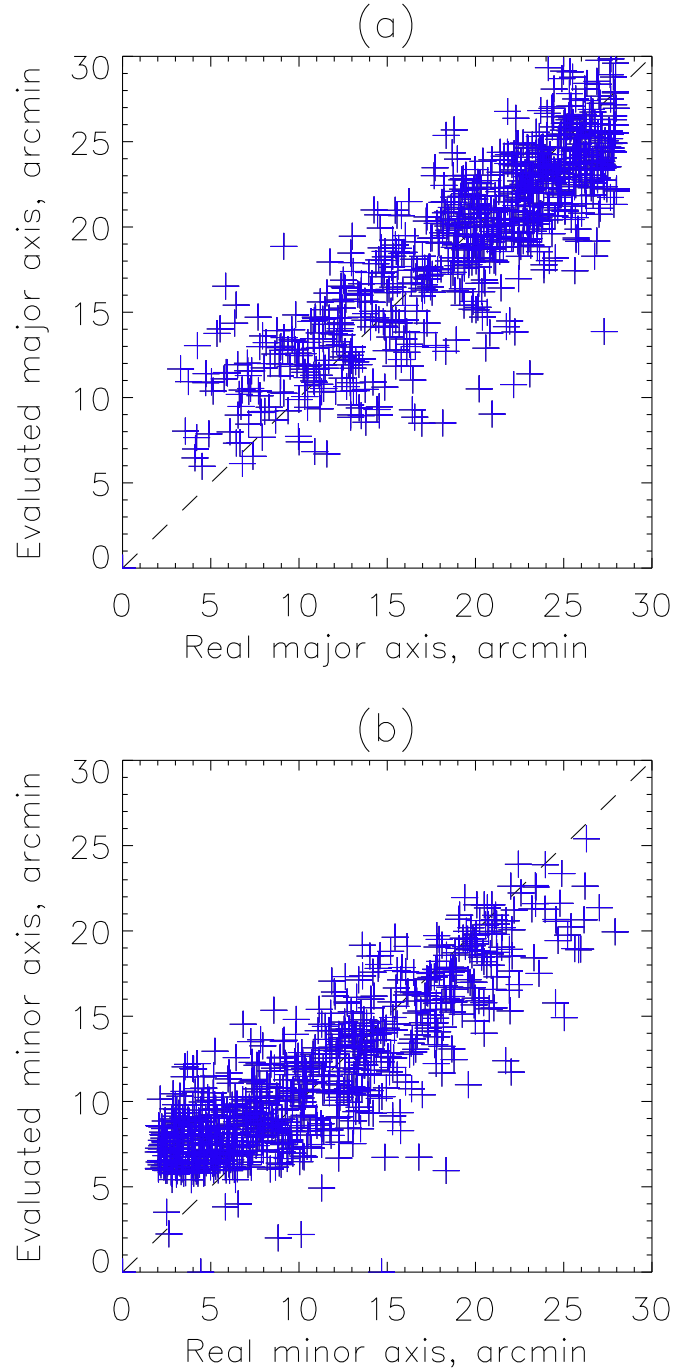


Figure 8. Comparison of the evaluated synthetic source sizes, major and minor axes of the half-maximum ellipses, with their actual values. The sizes were evaluated using the same set of procedures as used for solar data processing.

By comparing the derived parameters of the sources with their actual parameters (Figure 8) it was found that the error in minor and major axes measurements is $3'$. For an average source considered in this study, this error in size measurements would translate to an uncertainty in tilt angle measurements of about 15° – 20° . Although the error in centroid position estimated using the synthetic sources is only $1'$, in reality it is substantially larger, around $3'$ – $5'$, due to the variable ionospheric refraction (see Section 2.3, also Gordovskyy et al. 2019).

The constant background level estimation (Section 2.1) is another source of uncertainty. The assumption that at least 50%

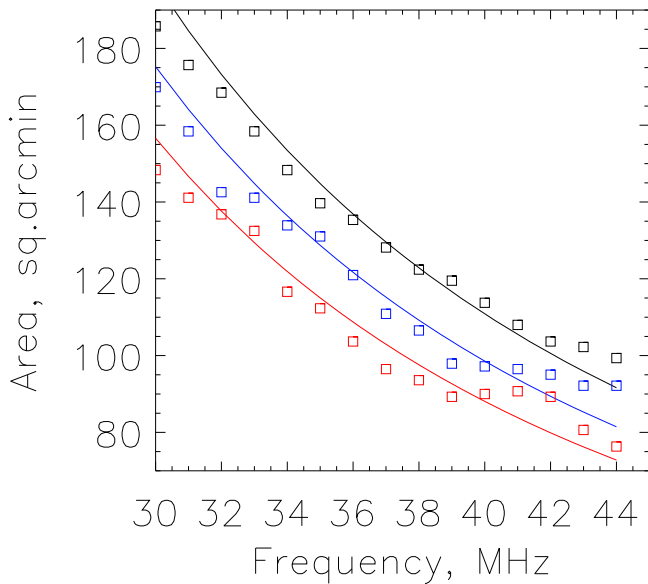


Figure 9. Area of the effective LOFAR PSF at zenith evaluated using different estimates for the constant background intensity. Black squares are for the PSF calculated with $N=2$, blue and red squares are for $N=109$ and $N=200$, respectively. Lines with corresponding colors show $1/f^2$ data fits.

of the field of view is free from *real* signal might be incorrect for large sources. Although this assumption should affect the synthetic source measurements done above, i.e., the error due to background uncertainty is included into the error estimated above, we evaluate separately the error due to the background level uncertainty. This is done by measuring Tau A areas assuming that only a small fraction of the field of view ($N=2$) is free from signal, and assuming that nearly the whole field of view is free from signal ($N=200$). As expected, the measured areas decrease with increasing N . However, this difference is moderate: for one example, the effective PSF area measured at 30 MHz with $N=2$ is about 18 arcmin^2 ($\sim 10\%$) bigger than the area measured with $N=109$, while the area measured with $N=200$ is approximately 17 arcmin^2 smaller than the area measured with $N=109$ (Figure 9). The resulting error in the measurements of solar source sizes caused by the uncertainty in the background intensity value is about $1/8$ i.e., significantly lower than the overall error ($\sim 2/5$ – $3/5$). This is because the background intensity is evaluated using the same approach and the same value of N both for Tau A and solar intensity maps, and the systematic errors in solar and Tau A measurements partially cancel each other.

3.4. Solar Source Sizes at Different Frequencies

The resulting sizes of the observed solar sources are shown in Figure 10. It can be noticed that at some frequencies, particularly above 40 MHz, the data is missing because the 2D Gaussian fitting procedure failed to converge. This may have happened for a number of reasons, including low signal, high noise level, or radio interference. However, where the data exists, it shows very similar patterns in most events.

The evaluated source sizes can be very different. Thus, at 30 MHz, the average sizes in the considered events range from $3'$ to about $15'$, although the majority of them (seven out of nine) are in a much smaller range between $8'$ and $12'$. One of the events (type III burst on 2017 July 13) has very small average size of about $3'$ (i.e., comparable to the error of size

measurements in this approach) at 30 MHz. At the same time, in one case (type IV event on 2015 June 20) the average source size at this frequency is about $15'$. In all considered events, the average sizes clearly decrease with increasing frequency, and can be approximated by a power law $\sim f^{-\gamma}$. For the majority of events, γ is between 1 and 2.

The evaluated shapes of solar radio sources show significant ellipticity, with the sizes of major axes being about a factor of 3 larger than the corresponding minor axis sizes. In seven out of nine considered events, the radial sizes are significantly smaller than the tangential sizes. At 30 MHz, the tangential sizes (which often nearly coincide with the major axes of the fitted Gaussians) are typically $10'$ – $20'$, while the sizes measured in radial direction are typically $5'$ – $10'$.

4. Discussion and Conclusions

In this study, we have achieved two major goals.

First, we have developed and tested a novel, simple method for deriving the PSF of an instrument based on known nearly point-like source observations at an arbitrary location. The derived method can be used for deconvolving intensity maps of the Sun or other bright radio objects, using a limited pool of calibration sources. This will enable an accurate analysis and interpretation of imaging observations obtained using instruments operating in TAB mode. We showed that the presented method works well, even at higher frequencies where LOFAR's TAB mode PSF has a rather complex structure. However, our tests also indicated that the known sources used for evaluating the instrument's PSF need to be observed with a field of view about twice as large as the field of view of the considered solar observations, in order to minimize the artefacts present near the field-of-view edges in the cleaned images.

The difference between the nominal and effective LOFAR PSFs is significant. In the 30–45 MHz range, the area of the effective PSF is about 1.6 times bigger than the nominal PSF area. Hence, using the nominal instead of the effective PSF may result in a significant overestimation of the intrinsic emission source sizes. Therefore, taking into account the unique role LOFAR is expected to play in the next few years in the exploration of the upper solar corona, evaluation of the effective LOFAR PSF and the PSF translation method are very important results in their own right. Furthermore, the developed method can be used for the analysis of imaging observations with future instruments, such as the Low-frequency Aperture Array of the Square Kilometer Array.

Second, for the first time, we have evaluated the intrinsic sizes and shapes of solar metric emission sources and their variation with frequency in the range 30–45 MHz. At 30 MHz, in seven out of nine events the average source sizes are between $8'$ and $12'$, which is around 2–4 times smaller than some previous observations, including observations with LOFAR. In seven out of the nine considered cases, the sources appear to be significantly smaller in the solar radial direction.

It is important to note that the considered sources of radio emission originate in radio bursts of different types. Although we believe that the observed emission is produced by the plasma mechanism because of its narrow bandwidth ($\Delta f/f \sim 0.1$), the physical sizes of the regions producing the observed emission, as well as the mechanisms of electron acceleration in these events are expected to be very different. Thus, type II and IV bursts are expected to be produced by large coronal structures, while physical volumes producing type III emission are expected to be

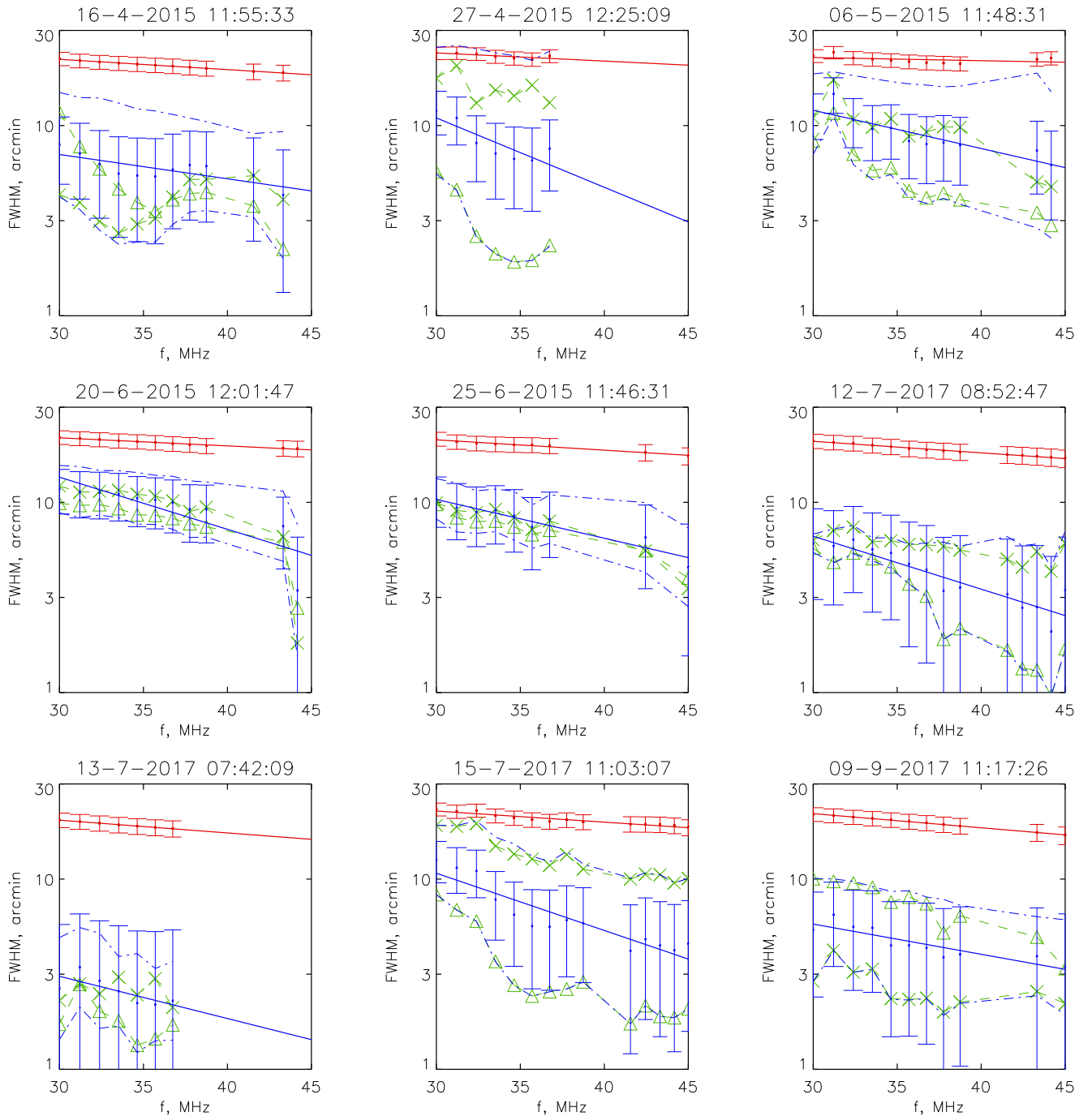


Figure 10. Sizes of solar radio sources observed at different frequencies by LOFAR in nine randomly selected separate events (dates and UT times are shown above the panels). Red dots with error bars show the average sizes of the brightest sources on dirty maps, while solid red lines show power-law fits ($af^{-\gamma}$). Similarly, blue dots with error bars show the average sizes of intrinsic sources, along with the power-law fits (solid blue lines). Blue dotted–dashed lines show the sizes of major and minor axes of the half-maximum ellipses corresponding to intrinsic sources. Green dashed lines with crosses and triangles show sizes of intrinsic sources in tangential and radial directions, respectively.

relatively small, comparable to the cross section of a magnetic flux tube in the upper corona (Kontar et al. 2017; Musset 2021). However, although out of nine considered events the smallest size corresponds to a type III burst (2017 July 13 event, Figure 10), while the largest (in terms of its average size) source corresponds to the type IV burst (2015 June 20 event), there is no systematic difference between type II and IV, and type III events.

Hence, at least for the considered type III events, one can say that the source sizes in solar radio bursts—even when corrected

for the effective PSF—are much larger than the expected intrinsic sizes of the emission sources. At the same time, the source sizes, their variation with frequency, and most importantly, ellipticities of the sources are consistent with the models of anisotropic radio-wave scattering in the corona and inner heliosphere (Kontar et al. 2019; Chen et al. 2020; Kuznetsov et al. 2020). Therefore, our findings support the concept that the sizes of low-frequency solar radio sources are determined primarily by radio-wave scattering in the upper corona, rather the physical sizes of the emitting regions.

M.G. and P.K.B. were supported by the Science and Technology Facilities Council (STFC, UK), grant ST/T00035X/1. D.L.C. and E.P.K. are thankful to DSTL for the funding through the UK-France PhD Scheme (contract DSTLX-1000106007). E.P.K. was supported by STFC consolidated grant ST/P000533/1. N.C. thanks CNES for its financial support. The authors acknowledge the support by the international team grant (<http://www.issibern.ch/teams/lofar/>) from ISSI Bern, Switzerland. This paper is based (in part) on data obtained from facilities of the International LOFAR Telescope (ILT) under project code LC3_012, LC4_016, and LC8_027. LOFAR van Haarlem et al. 2013 is the Low Frequency Array designed and constructed by ASTRON. It has observing, data processing, and data storage facilities in several countries, which are owned by various parties (each with their own funding sources), and that are collectively operated by the ILT foundation under a joint scientific policy. The ILT resources have benefited from the following recent major funding sources: CNRS-INSU, Observatoire de Paris and Université d'Orléans, France; BMBF, MIWF-NRW, MPG, Germany; Science Foundation Ireland (SFI), Department of Business, Enterprise and Innovation (DBEI), Ireland; NWO, The Netherlands; STFC, UK; Ministry of Science and Higher Education, Poland.

ORCID iDs

Mykola Gordovskyy  <https://orcid.org/0000-0003-2291-4922>
 Eduard P. Kontar  <https://orcid.org/0000-0002-8078-0902>
 Daniel L. Clarkson  <https://orcid.org/0000-0003-1967-5078>
 Nicolina Chrysaphi  <https://orcid.org/0000-0002-4389-5540>
 Philipp K. Browning  <https://orcid.org/0000-0002-7089-5562>

References

Abranin, E. P., Bazelian, L. L., Goncharov, N. I., et al. 1976, *SvA*, **19**, 602
 Abranin, E. P., Bazelian, L. L., Goncharov, N. I., et al. 1978, *SoPh*, **57**, 229

Barrow, C. H., Zarka, P., & Aubier, M. G. 1994, *A&A*, **286**, 597
 Bastian, T. S. 1994, *ApJ*, **426**, 774
 Bougeret, J. L., & Steinberg, J. L. 1977, *A&A*, **61**, 777
 Chen, H. S. L., & Shawhan, S. D. 1978, *SoPh*, **57**, 205
 Chen, X., Kontar, E. P., Chrysaphi, N., et al. 2020, *ApJ*, **905**, 43
 Chrysaphi, N., Kontar, E. P., Holman, G. D., & Temmer, M. 2018, *ApJ*, **868**, 79
 Chrysaphi, N., Reid, H. A. S., & Kontar, E. P. 2020, *ApJ*, **893**, 115
 de Jager, C., & Neven, L. 1966, *BAIN*, **18**, 306
 Dulk, G. A., Leblanc, Y., Robinson, P. A., Bougeret, J.-L., & Lin, R. P. 1998, *JGR*, **103**, 17223
 Ginzburg, V. L., & Zhelezniakov, V. V. 1958, *SvA*, **2**, 653
 Gordovskyy, M., Kontar, E., Browning, P., & Kuznetsov, A. 2019, *ApJ*, **873**, 48
 Högbom, J. A. 1974, *A&AS*, **15**, 417
 Hurford, G. J., Schmahl, E. J., Schwartz, R. A., et al. 2002, *SoPh*, **210**, 61
 Klein, K. L., Krucker, S., Trotter, G., & Hoang, S. 2005, *A&A*, **431**, 1047
 Kontar, E. P., Chen, X., Chrysaphi, N., et al. 2019, *ApJ*, **884**, 122
 Kontar, E. P., Yu, S., Kuznetsov, A. A., et al. 2017, *NatCo*, **8**, 1515
 Kundu, M. R. 1982, *RPPH*, **45**, 1435
 Kuznetsov, A. A., Chrysaphi, N., Kontar, E. P., & Motorina, G. 2020, *ApJ*, **898**, 94
 Kuznetsov, A. A., & Kontar, E. P. 2019, *A&A*, **631**, L7
 Magdalenic, J., Marqué, C., Fallows, R. A., et al. 2020, *ApJL*, **897**, L15
 Maloney, F. P., & Gottesman, S. T. 1979, *ApJ*, **234**, 485
 McLean, D. J., & Labrum, N. R. 1985, *Solar Radiophysics: Studies of Emission from the Sun at Metre Wavelengths* (New York: Cambridge Univ. Press)
 Mercier, C., & Jacobson, A. R. 1997, *AnGeo*, **15**, 430
 Mercier, C., Subramanian, P., Chambe, G., & Janardhan, P. 2015, *A&A*, **576**, A136
 Mercier, C., Subramanian, P., Kerdraon, A., et al. 2006, *A&A*, **447**, 1189
 Murphy, P. C., Carley, E. P., Ryan, A. M., Zucca, P., & Gallagher, P. T. 2021, *A&A*, **645**, A11
 Musset, S. 2021, arXiv:2101.07543
 Pick, M., & Vilmer, N. 2008, *A&ARv*, **16**, 1
 Reid, H. A. S., Vilmer, N., & Kontar, E. P. 2011, *A&A*, **529**, A66
 Sharykin, I. N., Kontar, E. P., & Kuznetsov, A. A. 2018, *SoPh*, **293**, 115
 Suzuki, S., & Dulk, G. A. 1985, *Bursts of Type III and Type V* (New York: Cambridge Univ. Press), 289
 van Haarlem, M. P., Wise, M. W., Gunst, A. W., et al. 2013, *A&A*, **556**, A2
 Warwick, J. W., & Dulk, G. A. 1969, *ApJL*, **158**, L123